Surface vibrational modes of the topological insulator Bi_2Se_3 observed by Raman spectroscopy

H.-H. Kung,[1,*] M. Salehi,[1,2] I. Boulares,[3] A. F. Kemper,[4] N. Koirala,[1] M. Brahlek,[1] P. Lošťák,[5] C. Uher,[3] R. Merlin,[3] X. Wang,[1,6] S.-W. Cheong,[1,6] S. Oh,[1] and G. Blumberg[1,7,†]

[1]*Department of Physics & Astronomy, Rutgers University, Piscataway, New Jersey 08854, USA*
[2]*Department of Materials Science and Engineering, Rutgers University, Piscataway, New Jersey 08854, USA*
[3]*Department of Physics, University of Michigan, Ann Arbor, Michigan 48109-1040, USA*
[4]*Department of Physics, North Carolina State University, Raleigh, North Carolina 27695, USA*
[5]*Faculty of Chemical Technology, University of Pardubice, Studentska 573, 53210 Pardubice, Czech Republic*
[6]*Rutgers Center for Emergent Materials, Rutgers University, Piscataway, New Jersey 08854, USA*
[7]*National Institute of Chemical Physics and Biophysics, 12618 Tallinn, Estonia*

(Received 17 November 2016; published 9 June 2017)

We present a polarization resolved Raman scattering study of surface vibration modes in the topological insulator Bi_2Se_3 single crystal and thick films. Besides the four Raman active bulk phonons, we observed four additional modes with much weaker intensity and slightly lower energy than the bulk counterparts. Using symmetry analysis, we assigned these additional modes to out-of-plane surface phonons. Comparing with first-principle calculations, we conclude that the appearance of these modes is due to *c*-axis lattice distortion and van der Waals gap expansion near the crystal surface. Two of the surface modes at 60 and 173 cm^{-1} are associated with Raman active A_{1g} bulk phonon modes, the other two at 136 and 158 cm^{-1} are associated with infrared active bulk phonons with A_{2u} symmetry. The latter become Raman allowed due to reduction of crystalline symmetry from D_{3d} in the bulk to C_{3v} on the crystal surface. In particular, the 158 cm^{-1} surface phonon mode shows a Fano line shape under resonant excitation, suggesting interference in the presence of electron-phonon coupling of the surface excitations.

DOI: 10.1103/PhysRevB.95.245406

I. INTRODUCTION

Topological insulators (TIs) are a new class of quantum matter characterized by linearly dispersed spin polarized gapless surface states within the bulk band gaps [1–8], which may lead to realization of novel phenomena and applications such as spintronics and quantum computing [8–17].

Despite the topological protection, the surface states away from the Dirac point suffer from hexagonal warping effect, resulting in increased scattering rate at the TI surface [18–20]. Among many possible inelastic scattering mechanisms, electron-phonon interaction is especially important due to its direct impact on device applications at finite temperature [21,22]. In particular, the self-energies and symmetries of the surface vibrational modes are essential for modeling the possible relaxation channels of the surface state excitations.

Theoretical modeling of surface lattice dynamics was first developed by Lifshitz and Rosenzweig [23,24], and later expanded by various workers [25–28]. The basic idea is to consider the free surface as a perturbation of an infinite lattice, and therefore to derive the surface modes from the spectrum of bulk vibrations. As a result, the frequencies of atomic vibration modes at the surface are modified to a smaller value than in the bulk at the Brillouin zone center (Γ point). If there is a gap in the phonon density-of-state (DOS) and with large enough distortion, the surface phonon DOS can be entirely separated from the bulk [23,26]. Such modes are long lived and localized at the surface, where the dispersion can be quite different than the bulk [29]. However, it is often experimentally challenging to distinguish surface signal from the overwhelmingly stronger intensity contribution of the bulk. Moreover, if the surface vibration mode is not completely gapped out from the bulk spectrum, then the surface and bulk modes are indistinguishable. Instead, the "bulk phonon" acquires only a slight energy shift near the crystal surface. Notice that the surface modes originate from abrupt termination of the lattice restoring force across bulk/vacuum interface in a semi-infinite crystal, and should not be confused with the phonons in quasi-two-dimensional (2D) ultrathin samples, which are almost decoupled from the underlying substrate of a different material [30–34].

Bi_2Se_3 is one of the most studied TIs due to its relatively simply band structure, i.e., a single Dirac cone within the 0.3 eV bulk band gap, much larger than the thermal energy at room temperature. While the bulk phonon modes have been extensively studied in Bi_2Se_3 single crystals [30,31,33–42], only a few papers have reported studies of the surface vibration modes. Zhu and co-workers observed strong Kohn anomaly at about $2k_F$ using helium atom scattering (HAS) [43], and deduced the interaction between surface phonon and the Dirac electrons to be much stronger than the values previously reported by angle-resolved photoemission spectroscopy (ARPES) measurements [19,44–46], suggesting that the electron-phonon coupling on a TI surface may be more complex than anticipated. Time-resolved ARPES study of single crystals reported the observation of one A_{1g} bulk phonon at about 74 cm^{-1}, and an additional mode with slightly lower energy consistent with what was suggested by transport measurements [22]. This mode was interpreted as a surface phonon associated with the observed A_{1g} bulk phonon [47]. However, alternative results have also been reported [19,46,48,49], suggesting the existence of multiple phononic decaying

*skung@physics.rutgers.edu
†girsh@physics.rutgers.edu

TABLE I. The list of single crystal and films measured in this study.

Sample	Composition	Description	Growth
2	Bi_2Se_3	50 QL thick film	MBE
8	$(Bi_2Se_3)_m(In_2Se_3)_n$	50 nm superlattice with $(m,n) = (5,5)$	MBE
10	$(Bi_2Se_3)_m(In_2Se_3)_n$	50 nm superlattice with $(m,n) = (10,5)$	MBE
13	$Bi_{1.95}In_{0.05}Se_3$	single crystal with indium doping	Bridgman
14	Bi_2Se_3	pristine single crystal	Bridgman
A	Bi_2Se_3	pristine single crystal	Bridgman

channels which may depend on details of sample preparation. An electron energy loss spectroscopy (EELS) study has distinguished a weak mode at about 160 cm^{-1} in Bi_2Se_3, which was assigned to the surface vibration mode associated with an A_{1g} bulk phonon [50]. The Raman scattering work on bulk single crystal [38] and exfoliated nanocrystals reported several additional features, and were attributed to infrared active phonon modes becoming Raman active due to inversion symmetry breaking at crystal surface [30,34].

To date, different surface modes were measured by several distinct spectroscopies, with slight discrepancies between the results and interpretations. To resolve the discrepancy, it is desirable to study all surface vibration modes within one technique that provides both high energy resolution and symmetry information.

Raman spectroscopy is a conventional tool for studying surface phonon modes [51,52]. Here we use high resolution polarization resolved Raman spectroscopy to study the vibrational modes in Bi_2Se_3 samples. We focus our study to the bulk single crystals, which are unexposed to air or any chemicals. In addition to the four Raman active bulk phonons, we observed six additional modes with about 20–100 times weaker intensities compared to the bulk phonons (Fig. 1). By comparing the data to the results obtained by the complementary spectroscopic techniques and the calculations, we assign the observed additional modes to surface phonons arising from out-of-plane lattice distortion near the crystal/film interface.

This paper is organized as follows. In Sec. II we introduce the experiments including sample preparations and the Raman probe. In Sec. III we present the low temperature polarized Raman spectra of bulk and thin film Bi_2Se_3 samples. Section IV discusses the symmetries and microscopic views of the surface vibration modes. Finally, we conclude our discussions in Sec. V. Details of data analysis are given in the Appendix.

II. EXPERIMENTAL SETUP

Table I lists six Bi_2Se_3 single crystals and films measured in this study. The bulk single crystals were grown by modified Bridgman method [53,54]. The thin film samples were epitaxially grown on Al_2O_3 (0001) substrates in a custom designed molecular beam epitaxy (MBE) chamber [55,56]. They were immediately transferred into a cryostat after being taken out of the MBE chamber.

The superlattice thin films of $(Bi_2Se_3)_m(In_2Se_3)_n$ are grown along (0001) surface [55], where each primitive cell consists of m quintuple layer (QL) Bi_2Se_3 and n QL In_2Se_3, with each QL being $\sim$ 1 nm thick. Notice that the light penetration depth in Bi_2Se_3 within energy range of the current study is about 10 nm [57]. Therefore, the signal is dominated by scattering from the first few QLs of Bi_2Se_3, and the scattering volume in the superlattice samples is practically the same as bulk.

Bi_2Se_3 has a rhombohedral crystal structure with the D_{3d} point group symmetry. The irreducible representations and Raman selection rules are given in Table II. With five atoms in a primitive unit cell, there are a total of three acoustic and 12 optical bulk phonon branches. At the Γ point, the irreducible representations of the Raman active phonons are $2A_{1g} + 2E_g$, and the infrared active phonons are $2A_{2u} + 2E_u$ [35,36]. These bulk phonon modes have been measured by Raman and infrared spectroscopies [30,31,33–42], and the values reported in Refs. [37,38] are listed in Table III.

The crystal naturally cleaves along the (111) surface terminated at Se atoms, forming optically flat QLs weakly bonded by van der Waals force [35]. The surface QL has the symmorphic $P6mm$ wallpaper group symmetry (two-dimensional crystallographic point group C_{6v}) [58–60]. Since the surface layer phonon modes in Bi_2Se_3 are not perfectly localized and decay into the bulk, it is more appropriate to analyze our experimental results within the layer group $P3m1$ (crystallographic point group C_{3v}, which is a subgroup containing common symmetry operators of D_{3d} and C_{6v} groups) [59].

All Raman scattering measurements are taken from ab surfaces freshly cleaved or grown immediately prior to the measurements. Samples 2–14 are measured in a quasibackscattering geometry in a continuous He-flow optical cryostat. A glove bag with a controlled dry nitrogen gas environment was sealed to the cryostat loading port. After purging the bag to the desired conditions, the single crystals were cleaved in the glove bag immediately before loading into the cryostat for cooling,

TABLE II. The Raman selection rules in the bulk and on the surface of Bi_2Se_3 [62,63]. Upon the reduction of symmetry from point group D_{3d} to C_{3v}, the A_{1g} and A_{2u} irreducible representations merge into A_1, A_{2g} and A_{1u} merge into A_2, E_g and E_u merge into E [64].

Scattering geometry	Bulk (D_{3d})	Surface (C_{3v})
RR	$A_{1g} + A_{2g}$	$A_1 + A_2$
RL	$2E_g$	$2E$
XX	$A_{1g} + E_g$	$A_1 + E$
YX	$A_{2g} + E_g$	$A_2 + E$

TABLE III. The summary of the bulk and surface phonon mode energies. This works data are compared to the spectroscopic studies reported in Refs. [30,31,33,34,37–42,47,50], and the calculations reported in Refs. [65,71]. All values are given in units of cm^{-1}.

	Experiment		Calculation	
Symmetry	This work	Literature	LDA+SOI [65]	GGA+SOI [71]
$A_{1g}^{(1)}$	75	73 [31,38,40,42]	77	64
$A_{1g}^{(2)}$	180	175 [31,38,40,42]	176	167
$E_{g}^{(1)}$	39	39 [31,38,40,42]	41	39
$E_{g}^{(2)}$	137	133 [31,38,40,42]	139	124
$A_{2u}^{(1)}$	–	N/A	139	137
$A_{2u}^{(2)}$	–	N/A	161	156
$E_{u}^{(1)}$	–	61 [37]	80	65
$E_{u}^{(2)}$	–	133 [37]	131	127
$A_{1}^{(1)}$	60	68 [47]	N/A	N/A
$A_{1}^{(2)}$	136	129 [38]	N/A	N/A
$A_{1}^{(3)}$	158	160 [38,50]	N/A	N/A
$A_{1}^{(4)}$	173	N/A	N/A	N/A
$E^{(1)}$	67	68 [38]	N/A	N/A
$E^{(2)}$	126	125 [38]	N/A	N/A

without exposure to air. We use a $\lambda_L = 532$ nm solid state laser for excitation, where the spot size is roughly 50 μm. The scattered light was analyzed and collected by a custom triple-grating spectrometer equipped with a liquid nitrogen cooled CCD detector.

As for the data collected from sample A, measurements were done in a backscattering geometry from a cold-finger cryostat. An argon ion laser and a Ti:sapphire laser were used as sources, where the spot sizes are roughly 35 and 55 μm, respectively. The scattered light was collected using a triple stage spectrometer (Dilor XY) and imaged on a CCD camera.

All spectra shown were corrected for the spectral response of the spectrometer and CCD to obtain the Raman intensity $I_{\mu\nu}(\omega,T)$, which is related to the Raman response function $\chi''_{\mu\nu}(\omega,T)$ by the Bose factor $n(\omega,T)$: $I_{\mu\nu}(\omega,T) = [1+n(\omega,T)]\chi''_{\mu\nu}(\omega,T)$. Here μ (ν) denotes the polarization of incident (scattered) photon, ω is energy, and T is temperature. The scattering geometries used in this experiment are denoted as $\mu\nu = RR, RL, XX$, and YX, which is short for $\bar{z}(\mu\nu)z$ in Porto's notation. $R = X + iY$ and $L = X - iY$ denotes the right- and left-circular polarizations, respectively, where X (Y) denotes linear polarization parallel (perpendicular) to the plane of incidence. The irreducible representations of the D_{3d} and C_{3v} groups corresponding to these scattering geometries are listed in Table II. Notice that in both the D_{3d} and C_{3v} groups, the phonon intensities do not depend on the orientation of the crystallographic axis. The notations X and Y have no reference to the crystallographic a and b axes. In order to avoid confusion with the weak surface modes, possible polarization leakage arising from optical elements are removed from the presented data with a procedure described in the Appendix.

III. RESULTS

Figure 1 shows the Raman response function $\chi''(\omega)$, taken at 13 K with 532 nm excitation, plot in semi-log scale. In order to confirm the tiny features of surface modes, we compared the results from bulk crystals and MBE films. Figures 1(a) and 1(b) are measured with the RR and RL scattering geometries, respectively (Table II). The dashed lines label the observed phonons as tabulated in Table III. The strong modes at 72 and 174 cm^{-1} in RR scattering geometry are the bulk A_{1g} phonons of Bi_2Se_3 [Fig. 1(a)], and the strong modes centered at 37 and 132 cm^{-1} in RL are the bulk E_g phonons [Fig. 1(b)], consistent with previous Raman studies [31,38] and calculations [65].

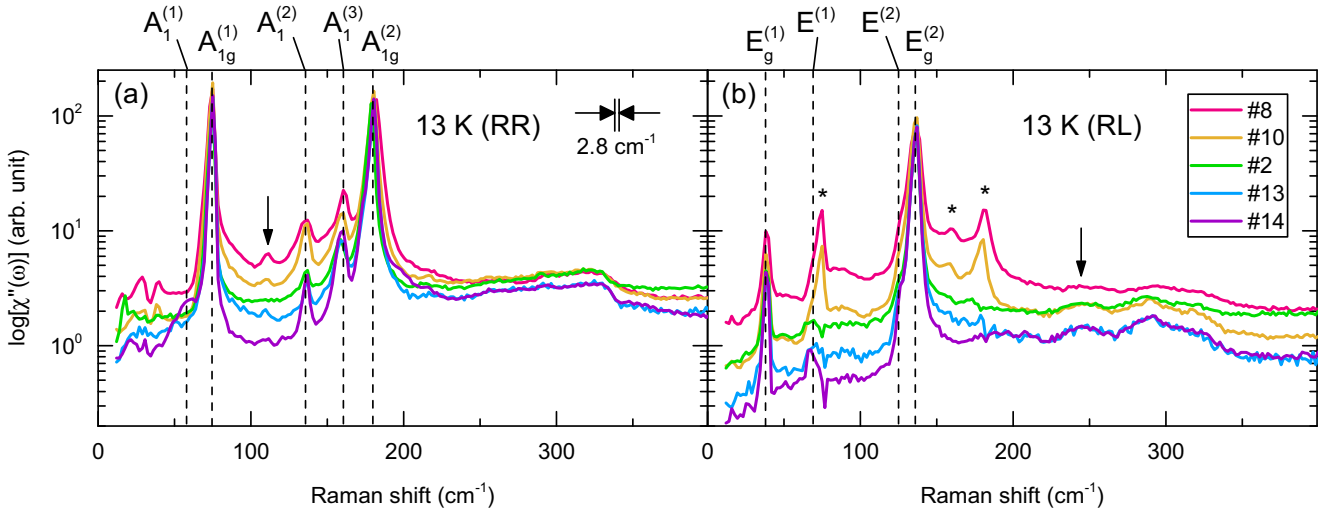

FIG. 1. The Raman response function $\chi''(\omega)$ measured in the (a) RR and (b) RL scattering geometry at 13 K with 532 nm excitation from various Bi_2Se_3 samples as described in Table I, plot in semi-log scale. The dashed lines label the observed phonon modes as tabulated in Table III. (a) The mode at 110 cm^{-1} indicated by an arrow is due to the phonon signal from $\alpha-In_2Se_3$ layers [61]. The asterisks mark the phonon modes with A_{1g} and A_1 symmetries, and appear in RL geometry due to indium atom diffusion. The instrumental resolution of 2.8 cm^{-1} is shown.

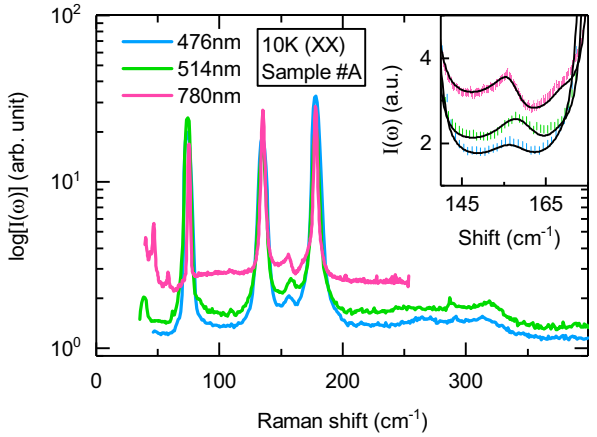

FIG. 2. The signal intensity in the XX scattering geometry, measured at 10 K from a bulk Bi_2Se_3 single crystal, plot in semi-log scale. The blue, green, and pink lines corresponds to laser excitation energy of 476, 514, and 780 nm, respectively. Inset: Enlarged plot around the $A_1^{(3)}$ mode. The black lines are fit to Fano line shape [Eq. (2)].

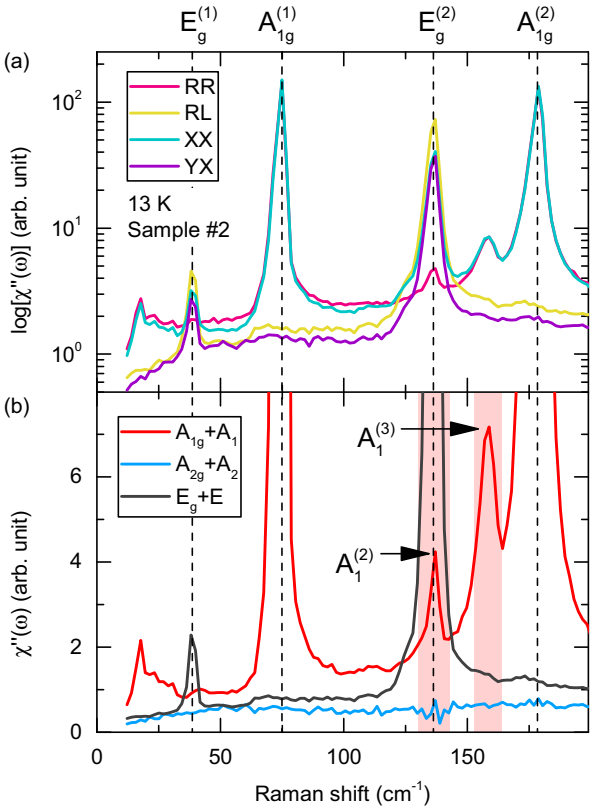

FIG. 3. (a) The Raman spectra taken in all four scattering geometries at 13 K with 532 nm excitation from a Bi_2Se_3 thick film, plotted on a semi-log scale. (b) The Raman response of different symmetry channels, obtained from data in (a). The bulk phonons are marked by dashed lines, whereas the surface modes are indicated by arrows and shaded in red.

The broad feature at about 330 cm^{-1} in RR is possibly due to second-order scattering of the $A_{1g}^{(2)}$ phonon, broadened due to the large downward dispersion of the phonon branch [65]. Similarly, the broad feature observed around 300 cm^{-1} in RL is assigned to two-phonon excitation $A_{1g}^{(2)} + E_g^{(2)}$. The broad feature at about 245 cm^{-1} [Fig. 1(b), marked by an arrow] was previously assigned to the 2D stretching mode of Se atoms on the surface [66]. However, we do not observe the reported resonance effect of this mode with near-infrared excitation (Fig. 2). Notice that this mode energy is also consistent with the two-phonon excitation of $A_{1g}^{(2)} + E_g^{(1)}$.

In order to distinguish the broad features from electronic origin, such as excitations from the topological surface states, we compared the results with indium doped Bi_2Se_3 in Fig. 1. Indium doping was shown to increase the carrier density and suppress the topological surface states in Bi_2Se_3 [55,67]. Here we collected data from bulk single crystals and MBE grown In_2Se_3/Bi_2Se_3 superlattices, where indium doping is achieved through diffusion in the superlattices [68]. In all indium doped samples, the broad features show the same intensity, suggesting their origin is unrelated to the topological surface states. This feature is slightly weaker in the superlattice sample 8, despite that the first-order phonon modes are still sharp and strong. However, this is likely mainly due to the indium atom diffusion into the Bi_2Se_3 layer, which breaks the translation symmetry, and therefore further broadens the multiphonon mode. The diffused indium atoms also lower the local crystal symmetry in the Bi_2Se_3 layers, and therefore allows vibration modes with A_{1g} and A_1 symmetries to appear in the RL geometry, which is otherwise forbidden for the crystal symmetry of Bi_2Se_3 [Fig. 1(b), marked by asterisks]. The small feature at 110 cm^{-1} in RR is due to a strong phonon of $\alpha-In_2Se_3$ layers [61] [indicated by an arrow in Fig. 1(a)].

In addition to the strong bulk first-order Raman phonons and the broad features, we see additional sharp modes that are about 20 times weaker than the bulk phonons. In Fig. 1(a) two such features at 136 and 158 cm^{-1} are seen in all samples in RR scattering geometry, labeled $A_1^{(2)}$ and $A_1^{(3)}$, respectively. In the bulk single crystal sample 14 we observed a mode at about 60 cm^{-1}, which we label as $A_1^{(1)}$. We associate these three features with vibration modes at the crystal surface, to be discussed in the RR polarization for sample 14 in the next section. We also noticed several sharp features below 50 cm^{-1} in samples 8 and 10 in RR, which are possibly zone folded phonons. To confirm this requires further studies, and is beyond the scope of this paper. In the RL scattering geometry, we observed two weak features at 67 and 126 cm^{-1}, labeled $E^{(1)}$ and $E^{(2)}$, respectively [Fig. 1(b)]. The energy of these modes are close to the strong bulk phonons, and therefore require higher resolution to distinguish them.

In Fig. 2 are the Raman spectra of the bulk sample at different excitation wavelengths at 10 K. The spectra were obtained in the XX polarization. As in Fig. 1, we observe an additional peak at 158 cm^{-1} which we refer to as $A_1^{(3)}$. However, note that the mode is more asymmetric when 780 nm excitation wavelength is used. This is an indication that the $A_1^{(3)}$ phonon is interacting with a continuum.

To further understand the observed phonon modes, we measure the Raman response in four scattering geometries of the D_{3d} and C_{3v} point group as listed in Table II [Fig. 3(a)].

The intensity contributed by each symmetry channel in different scattering geometries are dictated by the Raman tensors [62,63] and the results for D_{3d} and C_{3v} groups are listed in Table II. Therefore, by obtaining polarized Raman spectra in four proper scattering geometries, we can separate the measured Raman response from each symmetry channel:

$$\chi''_{A_{1g}}(\omega) + \chi''_{A_1}(\omega) = \chi''_{XX}(\omega) - \frac{1}{2}\chi''_{RL}(\omega),$$
$$\chi''_{A_{2g}}(\omega) + \chi''_{A_2}(\omega) = \chi''_{YX}(\omega) - \frac{1}{2}\chi''_{RL}(\omega),$$
$$\chi''_{E_g}(\omega) + \chi''_{E}(\omega) = \frac{1}{2}\chi''_{RL}(\omega). \quad (1)$$

The results are shown in Fig. 3(b). We notice that no lattice vibrational mode is observed in the A_{2g} and A_2 symmetry channels. This is because the Raman tensors for these two channels are antisymmetric and commonly correspond to pseudo-vector-like excitations [62,69,70], which is forbidden for phononic Raman scattering in Bi_2Se_3. Since the signal in A_{2g} and A_2 channels are expected to be zero, we can claim that all vibration modes appearing in RR have either A_{1g} or A_1 symmetry (Table II).

The $A_1^{(2)}$ mode happens to have energy very close to the $E_g^{(2)}$ phonon, making it particularly difficult for spectroscopic experiments to distinguish. Here we utilize the symmetry properties to separately detect them with polarized light. The polarization leakage of optical elements are precisely measured and removed (Appendix), and thereby excluding the possibility of $A_1^{(2)}$ being a trivial polarization leakage from the $E_g^{(2)}$ phonon.

To distinguish surface modes that are particularly weak and close in energy to the bulk phonons, we take high resolution spectra from a carefully prepared bulk crystal 14, cleaved in a nitrogen environment. We show in Fig. 4 the spectra taken at 13 K in RR and RL scattering geometries, where the smoother low resolution (2.8 cm^{-1}) data are overlapped with the high resolution (0.9 cm^{-1}) spectra. Besides the more pronounced $A_1^{(2)}$ and $A_1^{(3)}$ modes already visible in Fig. 3, we see a few additional features in the high resolution data: (1) A mode centered at 173 cm^{-1} appearing as a shoulder to the $A_{1g}^{(2)}$ bulk phonon in RR geometry [Fig. 4(a)], which we designate as $A_1^{(4)}$. (2) Another mode centered at 126 cm^{-1} appearing as a shoulder to the $E_g^{(2)}$ bulk phonon in RL geometry [Fig. 4(b)], which we designate as $E^{(2)}$. (3) The mode $A_1^{(3)}$ shows broadened peak structure. This cannot be due to splitting of an A-symmetry phonon, e.g., lowering of symmetry, since A_1 is a one-dimensional representation. This can be explained as due to Fano interference, which become more pronounced with infrared excitation (Fig. 2).

IV. DISCUSSION

At the crystal surface of Bi_2Se_3, the lattice structure is distorted along the c axis due to the abrupt reduction of the interlayer van der Waals force that binds the crystal together, and is calculated by density functional theory (DFT) to be about 10% along the c axis [47]. Additionally, the observation of a two-dimensional electron gas formed on a Bi_2Se_3 surface

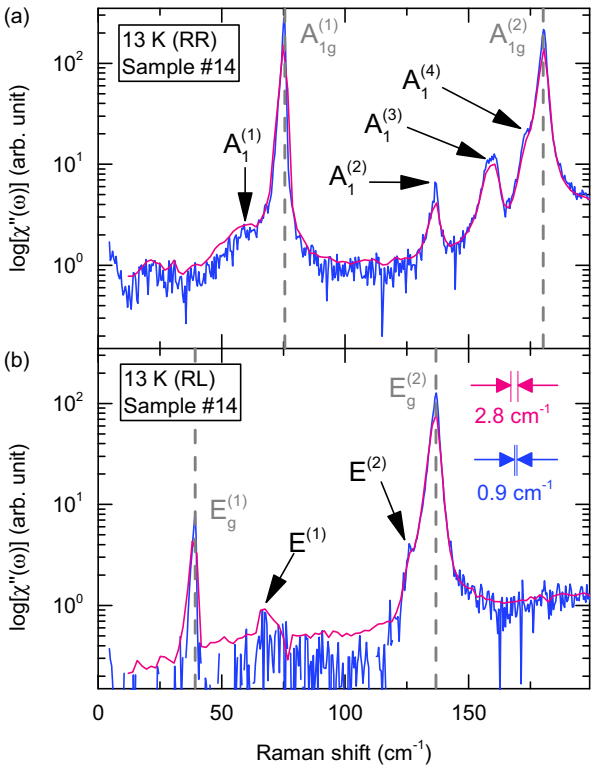

FIG. 4. The Raman spectra taken in the (a) RR and (b) RL scattering geometry at 13 K with 532 nm excitation from a bulk Bi_2Se_3 single crystal are plotted on a semi-log scale. The red and blue curves correspond to instrumental resolution of 2.8 and 0.9 cm^{-1} [as shown in (b)], respectively. The bulk phonons are marked by gray dashed lines.

also supports the picture of subsurface van der Waals gap expansion [6,72,73]. However, finite phonon DOS exist across the entire energy range in Bi_2Se_3 [65], allowing the surface modes to decay into bulk phonon modes. Therefore, the surface mode is not entirely "peeled off" from the bulk. Instead, one would expect a "surface resonance" with slightly lower energy than the bulk phonon.

Due to inversion symmetry breaking at the crystal interface, the surface resonance from the Raman active A_{1g} and IR active A_{2u} phonons are both expected to appear in the A_1 symmetry (C_{3v} group), corresponding to out-of-plane atomic motion. The energies of such surface modes are usually slightly lower than the corresponding bulk phonons. This is consistent with the four A_1 modes we observed [Fig. 4(a)]. From the energies of these A_1 modes, we conclude that $A_1^{(1)}$ and $A_1^{(4)}$ are associated with the bulk phonon modes $A_{1g}^{(1)}$ and $A_{1g}^{(2)}$, respectively. The measured energy of the $A_1^{(1)}$ mode is somewhat different than the previously reported value of 68 cm^{-1} by time resolved ARPES [47], but close to what was suggested by transport measurements [22]. We believe this difference may be partly due to surface quality variation. An ARPES measured sample is usually cleaved in ultrahigh vacuum, whereas the surface in this study is cleaved in a nitrogen environment. This may also explain why this mode was not observed in the MBE samples (Fig. 1), where the sample is unavoidably exposed to air for a few minutes during the transfer between MBE

chamber and Raman cryostat. The $A_1^{(4)}$ mode appears as a shoulder to the $A_{1g}^{(2)}$ bulk phonon, requiring higher resolution to distinguish from the bulk mode, and therefore was overlooked in the previous Raman study [38].

In comparison, the surface modes $A_1^{(2)}$ and $A_1^{(3)}$ have higher intensity and are better resolved. One possibility for this difference is that the bulk counterpart of these modes are the IR active $A_{2u}^{(1)}$ and $A_{2u}^{(2)}$ phonons, as the measured energy is close to the calculated values (Table III). Since these bulk modes are not Raman active, we were able to better resolve the surface resonance. Another possibility is that the phonon DOS is practically zero at these energies in the A_1 symmetry channel, and the surface vibration modes are truly localized. Distinguishing these two scenarios is in fact experimentally nontrivial, especially since the experimental values of the $A_{2u}^{(1)}$ and $A_{2u}^{(2)}$ bulk phonon energies are yet unknown.

Nevertheless, both possibilities point to the surface origin of these two modes, which provide us with information on the electron-phonon coupling at the TI surface. While the bulk phonons show little resonance effect, the $A_1^{(3)}$ phonon displays an antisymmetric line shape with 780 nm excitation, reminiscent of a Fano line shape [74] (Fig. 2, inset). This was overlooked in previous Raman studies, and may be related to the 20 meV "kink" in the topological surface state's energy dispersion curve reported by some ARPES measurements [48,49]. The observation of Fano line shape is a clear evidence for the existence of underlying electronic continuum in the A_1 symmetry channel, which interacts with the $A_1^{(3)}$ phonon [74,75]. The excitation dependence also suggests resonance enhancement of the electronic continuum with near-infrared wavelength, consistent with the reported surface states at about 1.6 eV above the Fermi energy [76,77]. Fitting the 780 nm data with Eq. 4.48 in Ref. [75]:

$$I(\omega) = \frac{\pi\rho T_e^2(\omega_0 - \omega - VT_p/T_e)^2}{(\omega_0 - \omega + V^2R)^2 + (\pi V^2\rho)^2}, \qquad (2)$$

yields electron-phonon interaction strength $V \approx 2.6$ cm^{-1}, and phonon energy $\omega_0 \approx 158$ cm^{-1}. Here we assumed the electron DOS ρ is a constant in the relevant energy window, and neglect the real part of the electronic Green's function R. T_p and T_e are the phonon and electronic continuum Raman transition matrix elements, respectively.

Since the in-plane symmetries are mainly preserved as the DFT calculated atomic surface distortion is purely out-of-plane [47], one would not expect surface phonon with E symmetry (C_{3v} group) for Bi_2Se_3. However, the in-plane bonding potential is also modified by having distortion along the c axis, and therefore the phonon frequency at surface is still slightly different than the bulk value. If the modification is tiny, the E modes are expected to be weak and close to the bulk phonons. In Figs. 1(b) and 4(b) we can see hints of two additional modes, labeled by $E^{(1)}$ and $E^{(2)}$. The energies of these modes are in fact close to the measured values of $E_u^{(1)}$ and $E_u^{(2)}$ bulk phonons [36,37], and are consistent with the previous Raman study [38] (Table III). However, the frequency of E_1 is slightly higher than $E_u^{(1)}$, which is against the expectation from a surface resonance. This may reflect the fact that this is an in-plane mode, orthogonal to the lattice distortion direction. Or, this may be indicative of nontrivial electron-phonon interaction with the surface states, and worth further studying.

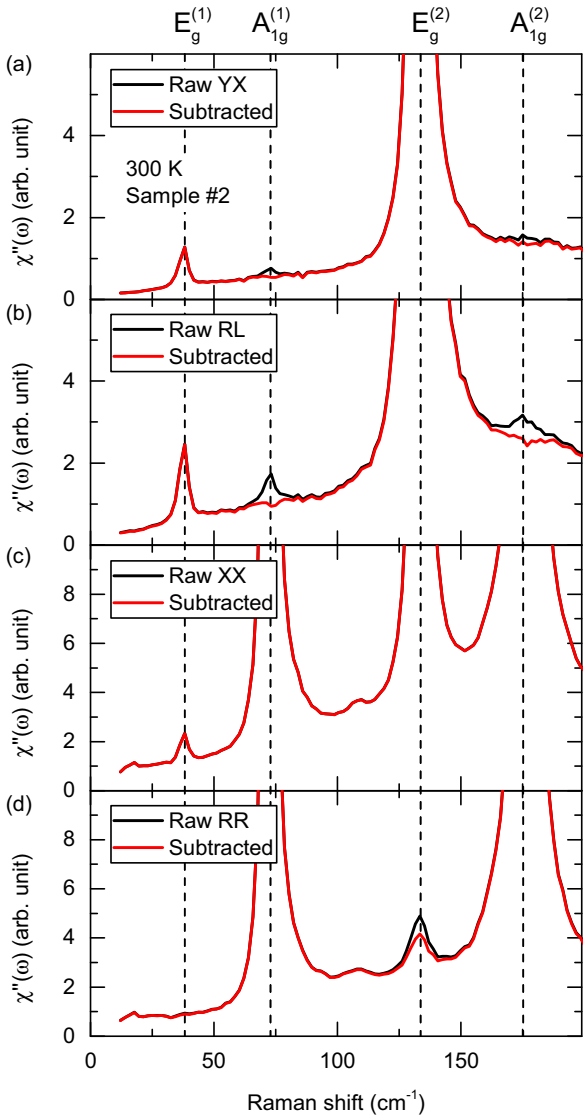

FIG. 5. Comparison of raw data and polarization leakage removed spectra, taken in (a) YX, (b) RL, (c) XX, and (d) RR polarization geometry from the ab surface of sample 2 at 300 K, with 532 nm excitation.

V. CONCLUSION

In conclusion, we have done a systematic symmetry analysis on the temperature and excitation dependent Raman spectra from high quality, freshly cleaved or grown ab surfaces of Bi_2Se_3 single crystal and films. We observed in total four out-of-plane, and possibly two in-plane surface vibrational modes, where we tabulate the energies and symmetries in Table III.

In particular, we reproduced the $A_1^{(1)}$ mode, which was previously observed in time resolved ARPES measurements [47]. The $A_1^{(1)}$ mode is interesting because it was found to couple strongly with the topological surface states, and therefore provides the main phononic decay channel for the Dirac fermions in Bi_2Se_3. Our report of energies and symmetries

of the $A_1^{(1)}$ and other surface modes affirms the validity of the surface lattice distortion model employed in Ref. [47]. The consistently much larger intensity for the out-of-plane vibration modes compared to in-plane modes strongly suggest that the surface lattice distortion and van der Waals gap expansion in Bi_2Se_3 is only along the c axis.

Lastly, the $A_1^{(2)}$ and $A_1^{(3)}$ modes have much stronger intensities compared to the other surface vibration modes, and may be candidates for localized surface phonons. In particular, we noticed the $A_1^{(3)}$ mode possesses a Fano line shape in low doped Bi_2Se_3 single crystals. The Fano line shape is indicative of electron-phonon coupling with the underlying electronic continuum of the same symmetry, important for understanding the relaxation and scattering of surface state excitations. Here we found a resonance effect to the Fano line shape with 780 nm excitation, suggesting the onset of the electronic continuum in A_1 symmetry has excitation dependence. This explains the inconsistent surface electron-phonon coupling constant found in previous ARPES studies [19,46]. The excitation dependence also confirms the existence of unoccupied surface states at about 1.6 eV above the Fermi energy, which enhances the surface electronic continuum through resonance effect.

ACKNOWLEDGMENTS

G.B. and H.-H.K acknowledge support from the U.S. DOE, BES Grant DE-SC0005463 for spectroscopic studies. S.O., M.S., N.K., and M.B. acknowledge support by Gordon and Betty Moore Foundation's EPiQS initiative (GBMF4418) and NSF (EFMA-1542798) for film growth. S.-W.C. and X.W. acknowledge support from NSF Award DMREF-1233349 for single crystal growth. G.B. also acknowledges partial support from QuantEmX grant from ICAM and the Gordon and Betty Moore Foundation through Grant GBMF5305 and from the European Regional Development Fund project TK134.

APPENDIX: REMOVAL OF POLARIZATION LEAKAGE

In this Appendix we explain the details of data analysis concerning removal of polarization leakage from optical elements. The degree of leakage are determined from the $A_{1g}^{(1)}$ and $A_{1g}^{(2)}$ bulk phonons of single crystal samples at room temperature. The removal of polarization leakage is done by subtracting intensity from the orthogonal polarization geometry, i.e., $\chi''_{YX}(\omega) = \overline{\chi''_{YX}}(\omega) - \alpha\overline{\chi''_{XX}}(\omega)$, where $\overline{\chi''_{YX}}(\omega)$ and $\overline{\chi''_{XX}}(\omega)$ are raw data taken in YX and XX polarization geometries, respectively, and α is the leakage ratio due to the limitations of polarization optics. It is reasonable to suggest that the same ratio also applies to XX polarization geometry: $\chi''_{XX}(\omega) = \overline{\chi''_{XX}}(\omega) - \alpha\overline{\chi''_{YX}}(\omega)$. Similarly, we have $\chi''_{RL}(\omega) = \overline{\chi''_{RL}}(\omega) - \beta\overline{\chi''_{RR}}(\omega)$ and $\chi''_{RR}(\omega) = \overline{\chi''_{RR}}(\omega) - \beta\overline{\chi''_{RL}}(\omega)$ for the circularly polarized geometries, where β is the leakage ratio due to the limitations of the broadband quarter wave plate and alignment of the Berek compensator. The ratios α and β are in general a weak function of ω, but in a narrow energy window as in this study, they can be safely assumed as constants. In order to avoid confusion from contributions of surface phonons, we chose YX and RL geometries as our reference for determination of α and β. In these two geometries, only $E_g^{(1)}$ and $E_g^{(2)}$ bulk phonons are expected to be present, the E symmetry surface modes are extremely weak and close to the bulk phonons (Fig. 4), and therefore do not raise concern for determination of α and β.

In Fig. 5 we show spectra of unprocessed raw data and polarization leakage removed results taken at 300 K from the ab surface of a Bi_2Se_3 thick film in black and red lines, respectively. The leakage intensity of $A_{1g}^{(1)}$ and $A_{1g}^{(2)}$ bulk phonons in raw data taken with YX and RL geometries can be fully removed with leakage ratios $\alpha = 0.004$ and $\beta = 0.015$, respectively. These values are within the specification of used broadband polarization optics.

The value of α depends only on the wavelength of light, and therefore the same value $\alpha = 0.004$ is used for all samples and temperatures measured with 532 nm excitation. The value of β depends critically on the alignment of the Berek compensator, which may vary between experiments, and has to be determined using the method described above in each experiment. In this study, the value of β is always within the range 0.015 ± 0.005.

[1] L. Fu, C. L. Kane, and E. J. Mele, Topological Insulators in Three Dimensions, Phys. Rev. Lett. **98**, 106803 (2007).

[2] H. Zhang, C.-X. Liu, X.-L. Qi, X. Dai, Z. Fang, and S.-C. Zhang, Topological insulators in Bi_2Se_3, Bi_2Te_3 and Sb_2Te_3 with a single Dirac cone on the surface, Nat. Phys. **5**, 438 (2009).

[3] D. Hsieh, Y. Xia, D. Qian, L. Wray, J. H. Dil, F. Meier, J. Osterwalder, L. Patthey, J. G. Checkelsky, N. P. Ong, A. V. Fedorov, H. Lin, A. Bansil, D. Grauer, Y. S. Hor, R. J. Cava, and M. Z. Hasan, A tunable topological insulator in the spin helical Dirac transport regime, Nature (London) **460**, 1101 (2009).

[4] Y. Xia, D. Qian, D. Hsieh, L. Wray, A. Pal, H. Lin, A. Bansil, D. Grauer, Y. S. Hor, R. J. Cava, and M. Z. Hasan, Observation of a large-gap topological-insulator class with a single Dirac cone on the surface, Nat. Phys. **5**, 398 (2009).

[5] J. G. Checkelsky, Y. S. Hor, M.-H. Liu, D.-X. Qu, R. J. Cava, and N. P. Ong, Quantum Interference in Macroscopic Crystals of Nonmetallic Bi_2Se_3, Phys. Rev. Lett. **103**, 246601 (2009).

[6] M. Bianchi, D. Guan, S. Bao, J. Mi, B. B. Iversen, P. D. C. King, and P. Hofmann, Coexistence of the topological state and a two-dimensional electron gas on the surface of Bi_2Se_3, Nat. Commun. **1**, 128 (2010).

[7] H. Beidenkopf, P. Roushan, J. Seo, L. Gorman, I. Drozdov, Y. S. Hor, R. J. Cava, and A. Yazdani, Spatial fluctuations of helical Dirac fermions on the surface of topological insulators, Nat. Phys. **7**, 939 (2011).

[8] M. Z. Hasan and J. E. Moore, Three-dimensional topological insulators, Annu. Rev. Condens. Matter Phys. **2**, 55 (2011).

[9] L. Fu and C. L. Kane, Superconducting Proximity Effect and Majorana Fermions at the Surface of a Topological Insulator, Phys. Rev. Lett. **100**, 096407 (2008).

[10] X.-L. Qi, T. L. Hughes, and S.-C. Zhang, Topological field theory of time-reversal invariant insulators, Phys. Rev. B **78**, 195424 (2008).

[11] X.-L. Qi, R. Li, J. Zang, and S.-C. Zhang, Inducing a magnetic monopole with topological surface states, Science **323**, 1184 (2009).

[12] M. Z. Hasan and C. L. Kane, *Colloquium*: Topological insulators, Rev. Mod. Phys. **82**, 3045 (2010).

[13] R. Yu, W. Zhang, H.-J. Zhang, S.-C. Zhang, X. Dai, and Z. Fang, Quantized anomalous Hall effect in magnetic topological insulators, Science **329**, 61 (2010).

[14] S. Raghu, S. B. Chung, X.-L. Qi, and S.-C. Zhang, Collective Modes of a Helical Liquid, Phys. Rev. Lett. **104**, 116401 (2010).

[15] X.-L. Qi and S.-C. Zhang, Topological insulators and superconductors, Rev. Mod. Phys. **83**, 1057 (2011).

[16] Y. H. Wang, H. Steinberg, P. Jarillo-Herrero, and N. Gedik, Observation of Floquet-Bloch states on the surface of a topological insulator, Science **342**, 453 (2013).

[17] T. Grover, D. N. Sheng, and A. Vishwanath, Emergent space-time supersymmetry at the boundary of a topological phase, Science **344**, 280 (2014).

[18] N. P. Butch, K. Kirshenbaum, P. Syers, A. B. Sushkov, G. S. Jenkins, H. D. Drew, and J. Paglione, Strong surface scattering in ultrahigh-mobility Bi_2Se_3 topological insulator crystals, Phys. Rev. B **81**, 241301 (2010).

[19] Z.-H. Pan, A. V. Fedorov, D. Gardner, Y. S. Lee, S. Chu, and T. Valla, Measurement of an Exceptionally Weak Electron-Phonon Coupling on the Surface of the Topological Insulator Bi_2Se_3 Using Angle-Resolved Photoemission Spectroscopy, Phys. Rev. Lett. **108**, 187001 (2012).

[20] T. Valla, Z.-H. Pan, D. Gardner, Y. S. Lee, and S. Chu, Photoemission Spectroscopy of Magnetic and Nonmagnetic Impurities on the Surface of the Bi_2Se_3 Topological Insulator, Phys. Rev. Lett. **108**, 117601 (2012).

[21] V. Parente, A. Tagliacozzo, F. von Oppen, and F. Guinea, Electron-phonon interaction on the surface of a three-dimensional topological insulator, Phys. Rev. B **88**, 075432 (2013).

[22] M. V. Costache, I. Neumann, J. F. Sierra, V. Marinova, M. M. Gospodinov, S. Roche, and S. O. Valenzuela, Fingerprints of Inelastic Transport at the Surface of the Topological Insulator Bi_2Se_3: Role of Electron-Phonon Coupling, Phys. Rev. Lett. **112**, 086601 (2014).

[23] I. M. Lifshitz and L. N. Rosenzweig, Dynamics of lattice filling half-space (Russian), Zh. Eksp. Teor. Fiz. **18**, 1012 (1948).

[24] I. M. Lifshitz, Some problems of the dynamic theory of non-ideal crystal lattices, Il Nuovo Cimento **3**, 716 (1956).

[25] R. F. Wallis, Effect of free ends on the vibration frequencies of one-dimensional lattices, Phys. Rev. **105**, 540 (1957).

[26] R. F. Wallis, Theory of surface modes of vibration in two- and three-dimensional crystal lattices, Phys. Rev. **116**, 302 (1959).

[27] G. Benedek and L. Miglio, The Green's function method in the surface lattice dynamics of ionic crystals, in *Surface Phonons*, edited by W. Kress and F. W. de Wette (Springer, Berlin, 1991), pp. 37–66.

[28] R. F. Wallis, Surface phonons: Theoretical developments, Surf. Sci. **299–300**, 612 (1994).

[29] M. J. Lagos, A. Trügler, U. Hohenester, and P. E. Batson, Mapping vibrational surface and bulk modes in a single nanocube, Nature (London) **543**, 529 (2017).

[30] S. Y. F. Zhao, C. Beekman, L. J. Sandilands, J. E. J. Bashucky, D. Kwok, N. Lee, A. D. LaForge, S. W. Cheong, and K. S. Burch, Fabrication and characterization of topological insulator Bi_2Se_3 nanocrystals, Appl. Phys. Lett. **98**, 141911 (2011).

[31] J. Zhang, Z. Peng, A. Soni, Y. Zhao, Y. Xiong, B. Peng, J. Wang, M. S. Dresselhaus, and Q. Xiong, Raman spectroscopy of few-quintuple layer topological insulator Bi_2Se_3 nanoplatelets, Nano Lett. **11**, 2407 (2011).

[32] V. Chis, I. Yu. Sklyadneva, K. A. Kokh, V. A. Volodin, O. E. Tereshchenko, and E. V. Chulkov, Vibrations in binary and ternary topological insulators: First-principles calculations and Raman spectroscopy measurements, Phys. Rev. B **86**, 174304 (2012).

[33] J. Humlíček, D. Hemzal, A. Dubroka, O. Caha, H. Steiner, G. Bauer, and G. Springholz, Raman and interband optical spectra of epitaxial layers of the topological insulators Bi_2Te_3 and Bi_2Se_3 on BaF_2 substrates, Phys. Scr. **2014**, 014007 (2014).

[34] M. Eddrief, P. Atkinson, V. Etgens, and B. Jusserand, Low-temperature Raman fingerprints for few-quintuple layer topological insulator Bi_2Se_3 films epitaxied on GaAs, Nanotechnology **25**, 245701 (2014).

[35] H. Köhler and C. R. Becker, Optically active lattice vibrations in Bi_2Se_3, Phys. Status Solidi (b) **61**, 533 (1974).

[36] W. Richter and C. R. Becker, A Raman and far-infrared investigation of phonons in the rhombohedral V_2VI_3 compounds Bi_2Te_3, Bi_2Se_3, Sb_2Te_3 and $Bi_2(Te_{1-x}Se_x)_3$ $(0 < x < 1)$, $(Bi_{1-y}Sb_y)_2Te_3$ $(0 < y < 1)$, Phys. Status Solidi (b) **84**, 619 (1977).

[37] A. D. LaForge, A. Frenzel, B. C. Pursley, T. Lin, X. Liu, J. Shi, and D. N. Basov, Optical characterization of Bi_2Se_3 in a magnetic field: Infrared evidence for magnetoelectric coupling in a topological insulator material, Phys. Rev. B **81**, 125120 (2010).

[38] V. Gnezdilov, Y. G. Pashkevich, H. Berger, E. Pomjakushina, K. Conder, and P. Lemmens, Helical fluctuations in the Raman response of the topological insulator Bi_2Se_3, Phys. Rev. B **84**, 195118 (2011).

[39] Y. Kim, X. Chen, Z. Wang, J. Shi, I. Miotkowski, Y. P. Chen, P. A. Sharma, A. L. L. Sharma, M. A. Hekmaty, Z. Jiang, and D. Smirnov, Temperature dependence of Raman-active optical phonons in Bi_2Se_3 and Sb_2Te_3, Appl. Phys. Lett. **100**, 071907 (2012).

[40] B. Irfan, S. Sahoo, A. P. S. Gaur, M. Ahmadi, M. J.-F. Guinel, R. S. Katiyar, and R. Chatterjee, Temperature dependent Raman scattering studies of three dimensional topological insulators Bi_2Se_3, J. Appl. Phys. **115**, 173506 (2014).

[41] Y. Yan, X. Zhou, H. Jin, C.-Z. Li, X. Ke, G. Van Tendeloo, K. Liu, D. Yu, M. Dresselhaus, and Z.-M. Liao, Surface-facet-dependent phonon deformation potential in individual strained topological insulator Bi_2Se_3 nanoribbons, ACS Nano **9**, 10244 (2015).

[42] X. Zhang, Q.-H. Tan, J.-B. Wu, W. Shi, and P.-H. Tan, Review on the Raman spectroscopy of different types of layered materials, Nanoscale **8**, 6435 (2016).

[43] X. Zhu, L. Santos, R. Sankar, S. Chikara, C. Howard, F. C. Chou, C. Chamon, and M. El-Batanouny, Interaction of Phonons and Dirac Fermions on the Surface of Bi_2Se_3: A Strong Kohn Anomaly, Phys. Rev. Lett. **107**, 186102 (2011).

[44] X. Zhu, L. Santos, C. Howard, R. Sankar, F. C. Chou, C. Chamon, and M. El-Batanouny, Electron-Phonon Coupling on the Surface of the Topological Insulator Bi_2Se_3 Determined from Surface-Phonon Dispersion Measurements, Phys. Rev. Lett. **108**, 185501 (2012).

[45] C. Howard, M. El-Batanouny, R. Sankar, and F. C. Chou, Anomalous behavior in the phonon dispersion of the (001) surface of Bi_2Te_3 determined from helium atom-surface scattering measurements, Phys. Rev. B **88**, 035402 (2013).

[46] R. C. Hatch, M. Bianchi, D. Guan, S. Bao, J. Mi, B. B. Iversen, L. Nilsson, L. Hornekær, and P. Hofmann, Stability of the Bi_2Se_3(111) topological state: Electron-phonon and electron-defect scattering, Phys. Rev. B **83**, 241303(R) (2011).

[47] J. A. Sobota, S.-L. Yang, D. Leuenberger, A. F. Kemper, J. G. Analytis, I. R. Fisher, P. S. Kirchmann, T. P. Devereaux, and Z.-X. Shen, Distinguishing Bulk and Surface Electron-Phonon Coupling in the Topological Insulator Bi_2Se_3 Using Time-Resolved Photoemission Spectroscopy, Phys. Rev. Lett. **113**, 157401 (2014).

[48] C. Chen, Z. Xie, Y. Feng, H. Yi, A. Liang, S. He, D. Mou, J. He, Y. Peng, X. Liu, Y. Liu, L. Zhao, G. Liu, X. Dong, J. Zhang, L. Yu, X. Wang, Q. Peng, Z. Wang, S. Zhang, F. Yang, C. Chen, Z. Xu, and X. J. Zhou, Tunable Dirac fermion dynamics in topological insulators, Sci. Rep. **3**, 2411 (2013).

[49] T. Kondo, Y. Nakashima, Y. Ota, Y. Ishida, W. Malaeb, K. Okazaki, S. Shin, M. Kriener, S. Sasaki, K. Segawa, and Y. Ando, Anomalous Dressing of Dirac Fermions in the Topological Surface State of Bi_2Se_3, Bi_2Te_3, and Cu-Doped Bi_2Se_3, Phys. Rev. Lett. **110**, 217601 (2013).

[50] A. Kogar, S. Vig, A. Thaler, M. H. Wong, Y. Xiao, D. Reig-i-Plessis, G. Y. Cho, T. Valla, Z. Pan, J. Schneeloch, R. Zhong, G. D. Gu, T. L. Hughes, G. J. MacDougall, T.-C. Chiang, and P. Abbamonte, Surface Collective Modes in the Topological Insulators Bi_2Se_3 and $Bi_{0.5}Sb_{1.5}Te_{3-x}Se_x$, Phys. Rev. Lett. **115**, 257402 (2015).

[51] N. Esser and W. Richter, Raman scattering from surface phonons, in *Light Scattering in Solids VIII*, edited by M. Cardona and G. Güntherodt (Springer, Berlin, 1999), pp. 96–168.

[52] M. Liebhaber, U. Bass, P. Bayersdorfer, J. Geurts, E. Speiser, J. Räthel, A. Baumann, S. Chandola, and N. Esser, Surface phonons of the Si(111)-(7 × 7) reconstruction observed by Raman spectroscopy, Phys. Rev. B **89**, 045313 (2014).

[53] P. Lošťák, L. Beneš, S. Civiš, and H. Süssmann, Preparation and some physical properties of $Bi_{2x}In_xSe_3$ single crystals, J. Mater. Sci. **25**, 277 (1990).

[54] J. Dai, D. West, X. Wang, Y. Wang, D. Kwok, S.-W. Cheong, S. B. Zhang, and W. Wu, Toward the Intrinsic Limit of the Topological Insulator Bi_2Se_3, Phys. Rev. Lett. **117**, 106401 (2016).

[55] M. Brahlek, N. Bansal, N. Koirala, S.-Y. Xu, M. Neupane, C. Liu, M. Z. Hasan, and S. Oh, Topological-Metal to Band-Insulator Transition in $(Bi_{1-x}In_x)_2Se_3$ Thin Films, Phys. Rev. Lett. **109**, 186403 (2012).

[56] N. Bansal, Y. S. Kim, M. Brahlek, E. Edrey, and S. Oh, Thickness-Independent Transport Channels in Topological Insulator Bi_2Se_3 Thin Films, Phys. Rev. Lett. **109**, 116804 (2012).

[57] J. W. McIver, D. Hsieh, H. Steinberg, P. Jarillo-Herrero, and N. Gedik, Control over topological insulator photocurrents with light polarization, Nat. Nanotechnol. **7**, 96 (2012).

[58] T. Terzibaschian and B. Enderlein, The irreducible representations of the two-dimensional space groups of crystal surfaces. Theory and applications, Phys. Status Solidi (b) **133**, 443 (1986).

[59] J. Li, J. J. Tu, and J. L. Birman, Symmetry predicted transitions in 3D topological insulators, Solid State Commun. **163**, 11 (2013).

[60] R.-J. Slager, A. Mesaros, V. Juričić, and J. Zaanen, The space group classification of topological band-insulators, Nat. Phys. **9**, 98 (2013).

[61] R. Lewandowska, R. Bacewicz, J. Filipowicz, and W. Paszkowicz, Raman scattering in $\alpha-In_2Se_3$ crystals, Mater. Res. Bull. **36**, 2577 (2001).

[62] L. N. Ovander, The form of the Raman tensor, Opt. Spectrosc. **9**, 302 (1960).

[63] M. Cardona, Resonance phenomena, in *Light scattering in Solids II*, edited by M. Cardona and G. Güntherodt (Springer, Berlin, 1982), pp. 45–49.

[64] G. F. Koster, *Properties of the Thirty-Two Point Groups*, Massachusetts Institute of Technology Research Monograph (M.I.T. Press, Cambridge, 1963).

[65] B.-T. Wang and P. Zhang, Phonon spectrum and bonding properties of Bi_2Se_3: Role of strong spin-orbit interaction, Appl. Phys. Lett. **100**, 082109 (2012).

[66] Y. D. Glinka, S. Babakiray, T. A Johnson, and D. Lederman, Thickness tunable quantum interference between surface phonon and Dirac plasmon states in thin films of the topological insulator Bi_2Se_3, J. Phys.: Condens. Matter **27**, 052203 (2015).

[67] L. Wu, M. Brahlek, R. Valdes Aguilar, A. V. Stier, C. M. Morris, Y. Lubashevsky, L. S. Bilbro, N. Bansal, S. Oh, and N. P. Armitage, A sudden collapse in the transport lifetime across the topological phase transition in $(Bi_{1-x}\ In_x)_2Se_3$, Nat. Phys. **9**, 410 (2013).

[68] H. D. Lee, C. Xu, S. M. Shubeita, M. Brahlek, N. Koirala, S. Oh, and T. Gustafsson, Indium and bismuth interdiffusion and its influence on the mobility in In_2Se_3/Bi_2Se_3, Thin Solid Films **556**, 322 (2014).

[69] B. S. Shastry and B. I. Shraiman, Raman scattering in Mott-Hubbard systems, Int. J. Mod. Phys. B **05**, 365 (1991).

[70] D. V. Khveshchenko and P. B. Wiegmann, Raman Scattering and Anomalous Current Algebra in Mott Insulators, Phys. Rev. Lett. **73**, 500 (1994).

[71] W. Cheng and S.-F. Ren, Phonons of single quintuple Bi_2Te_3 and Bi_2Se_3 films and bulk materials, Phys. Rev. B **83**, 094301 (2011).

[72] M. Bianchi, R. C. Hatch, D. Guan, T. Planke, J. Mi, B. B. Iversen, and P. Hofmann, The electronic structure of clean and adsorbate-covered Bi_2Se_3: An angle-resolved photoemission study, Semicond. Sci. Technol. **27**, 124001 (2012).

[73] T. V. Menshchikova, S. V. Eremeev, and E. V. Chulkov, On the origin of two-dimensional electron gas states at the surface of topological insulators, JETP Lett. **94**, 106 (2011).

[74] U. Fano, Effects of configuration interaction on intensities and phase shifts, Phys. Rev. **124**, 1866 (1961).

[75] M. V. Klein, Electronic raman scattering, in *Light Scattering in Solids I*, edited by M. Cardona and G. Güntherodt (Springer, Berlin, 1983), pp. 169–172.

[76] J. A. Sobota, S.-L. Yang, A. F. Kemper, J. J. Lee, F. T. Schmitt, W. Li, R. G. Moore, J. G. Analytis, I. R. Fisher, P. S. Kirchmann, T. P. Devereaux, and Z.-X. Shen, Direct Optical Coupling to an Unoccupied Dirac Surface State in the Topological Insulator Bi_2Se_3, Phys. Rev. Lett. **111**, 136802 (2013).

[77] D. Niesner, T. Fauster, S. V. Eremeev, T. V. Menshchikova, Y. M. Koroteev, A. P. Protogenov, E. V. Chulkov, O. E. Tereshchenko, K. A. Kokh, O. Alekperov, A. Nadjafov, and N. Mamedov, Unoccupied topological states on bismuth chalcogenides, Phys. Rev. B **86**, 205403 (2012).